Medical Physics
The International Journal of Medical Physics Research and Practice

Simulating cardiac ultrasound image based on MR diffusion tensor imaging

Xulei Qin, Silun Wang, Ming Shen, Guolan Lu, Xiaodong Zhang, Mary B. Wagner, and Baowei Fei

Citation: Medical Physics **42**, 5144 (2015); doi: 10.1118/1.4927788
View online: http://dx.doi.org/10.1118/1.4927788
View Table of Contents: http://scitation.aip.org/content/aapm/journal/medphys/42/9?ver=pdfcov
Published by the American Association of Physicists in Medicine

Simulating cardiac ultrasound image based on MR diffusion tensor imaging

Xulei Qin
Department of Radiology and Imaging Sciences, Emory University School of Medicine, Atlanta, Georgia 30329

Silun Wang
Yerkes Imaging Center, Yerkes National Primate Research Center, Emory University, Atlanta, Georgia 30329

Ming Shen
Emory University Department of Pediatrics and Children's Healthcare of Atlanta, Atlanta, Georgia 30322

Guolan Lu
Department of Biomedical Engineering, Emory University and Georgia Institute of Technology, Atlanta, Georgia 30329

Xiaodong Zhang
Yerkes Imaging Center, Yerkes National Primate Research Center, Emory University, Atlanta, Georgia 30329

Mary B. Wagner
Emory University Department of Pediatrics and Children's Healthcare of Atlanta, Atlanta, Georgia 30322

Baowei Fei[a)]
Department of Radiology and Imaging Sciences, Emory University School of Medicine, Atlanta, Georgia 30329; Department of Mathematics and Computer Science, Emory University, Atlanta, Georgia 30329; and Department of Biomedical Engineering, Emory University and Georgia Institute of Technology, Atlanta, Georgia 30329

(Received 2 April 2015; revised 14 July 2015; accepted for publication 21 July 2015; published 11 August 2015)

Purpose: Cardiac ultrasound simulation can have important applications in the design of ultrasound systems, understanding the interaction effect between ultrasound and tissue and setting the ground truth for validating quantification methods. Current ultrasound simulation methods fail to simulate the myocardial intensity anisotropies. New simulation methods are needed in order to simulate realistic ultrasound images of the heart.
Methods: The proposed cardiac ultrasound image simulation method is based on diffusion tensor imaging (DTI) data of the heart. The method utilizes both the cardiac geometry and the fiber orientation information to simulate the anisotropic intensities in B-mode ultrasound images. Before the simulation procedure, the geometry and fiber orientations of the heart are obtained from high-resolution structural MRI and DTI data, respectively. The simulation includes two important steps. First, the backscatter coefficients of the point scatterers inside the myocardium are processed according to the fiber orientations using an anisotropic model. Second, the cardiac ultrasound images are simulated with anisotropic myocardial intensities. The proposed method was also compared with two other nonanisotropic intensity methods using 50 B-mode ultrasound image volumes of five different rat hearts. The simulated images were also compared with the ultrasound images of a diseased rat heart *in vivo*. A new segmental evaluation method is proposed to validate the simulation results. The average relative errors (AREs) of five parameters, i.e., mean intensity, Rayleigh distribution parameter σ, and first, second, and third quartiles, were utilized as the evaluation metrics. The simulated images were quantitatively compared with real ultrasound images in both *ex vivo* and *in vivo* experiments.
Results: The proposed ultrasound image simulation method can realistically simulate cardiac ultrasound images of the heart using high-resolution MR-DTI data. The AREs of their proposed method are 19% for the mean intensity, 17.7% for the scale parameter of Rayleigh distribution, 36.8% for the first quartile of the image intensities, 25.2% for the second quartile, and 19.9% for the third quartile. In contrast, the errors of the other two methods are generally five times more than those of their proposed method.
Conclusions: The proposed simulation method uses MR-DTI data and realistically generates cardiac ultrasound images with anisotropic intensities inside the myocardium. The ultrasound simulation method could provide a tool for many potential research and clinical applications in cardiac ultrasound imaging. [http://dx.doi.org/10.1118/1.4927788]

Key words: cardiac ultrasound simulation, intensity anisotropy, diffusion tensor imaging, anisotropic modeling

1. INTRODUCTION

Cardiac ultrasound imaging, also called echocardiography, is one of the most widely used examinations in cardiology. Simulation of cardiac ultrasound images plays important roles in the design of ultrasound systems and parameter optimization,[1] understanding the interaction effect between ultrasound and cardiac tissue[2,3] and setting the ground truth for validating quantification methods.[4–7]

In order to simulate the tissue scattering in B-mode ultrasound, different models have been proposed to approximate the probability density of ultrasound speckle.[2] These models, such as Rayleigh,[8] Rician,[9] and Nakagami distributions,[3] were proposed by considering different aspects during ultrasound speckle generation at the transducer. Moreover, a group of empirical probability distribution models for speckle density in the B-mode images was also evaluated by clinical cardiac ultrasound images.[10] These models are widely used in ultrasound simulation, speckle reduction, and segmentations.[7,11] Moreover, several ultrasound simulators were developed. Field II is a well-known simulation method that linearly calculates the impulse responses of all scatterers.[1] However, the spatial response methods are usually very time-consuming. Thus, an acceleration step by decreasing the simulated accuracy was proposed by convolving an object with a point-spread function (PSF). A fast ultrasound imaging simulation in *K*-space (FUSK) was designed by Hergum *et al.* specifically for three dimensional (3D) cardiac ultrasound series simulations, which is much faster than Field II but maintains the similar speckle patterns.[12] Another simulator called COLE was developed to accelerate the convolution of a 3D point-spread function by multiple 1D convolution.[13] Meanwhile, it also allowed the integration of various simulated or measured beam profiles as a lookup table.

Simulation technologies were applied to provide the ground truths to evaluate different cardiac quantification methods. Zhu *et al.* generated 3D synthetic series by Field II to validate the accuracy of their myocardial border detection method.[7] Simulation was also utilized to evaluate the fiber structure measurements from high-frequency ultrasound.[14] COLE was applied to simulate the 3D geometries of left ventricle, which were utilized to validate their strain estimation.[4,5,15] FUSK was also applied to validate the assessment of left ventricle function.[16] Furthermore, various efforts were made on providing gold standards for echocardiography strain analysis.[17–19] In order to simulate more realistic ventricular geometries and motion, Duan *et al.* integrated an electromechanical model in the simulations.[20] Similar to this idea, a biomechanical model based simulation method was used to evaluate a sparse demons registration for calculating 3D cardiac motion and strain.[15] Based on these methods, a database that simulated healthy, ischemic and dyssynchrony cases was generated and used to evaluate five different 3D ultrasound tracking algorithms.[5] Based on the generated motion field, another framework was proposed to directly warp the real ultrasound sequence to generate a new sequence.[21,22]

Current simulation methods generate the myocardium as a cloud of scatterers and did not consider anisotropic effects that exist in the real cardiac ultrasound images. Moreover, cardiac ultrasound imaging, especially in the short axis view, usually contains anisotropic phenomena that severely affect the intensity homogeneity as shown in Fig. 1(a), which could lead to inaccuracy of cardiac segmentation or speckle tracking.[23] The relationships between ultrasound intensities and anisotropic microstructures of myocardium have been investigated since last 1970s.[24] For example, Miller and coworkers thoroughly investigated the relationship between myocardial anisotropy and echocardiography intensities.[25–31] These studies indicate that the anisotropic intensities mainly relate to the variable cardiac fiber orientations: the orientations that are parallel to the ultrasound beams lead to the lowest intensities and those that are perpendicular to the beam lead to the highest intensities, as shown in Figs. 1(b) and 1(c). A statistical parametric model of the myocardial anisotropy was developed by modeling the myocardium as a matrix of cylindrical scatterers.[32] Crosby *et al.* further qualitatively demonstrated the feasibility of simulating the anisotropy in ultrasound images with special designed tissue structures.[23] However, how to accurately perform these anisotropies in the simulation of the complicated architectures of a real heart and how to quantify their accuracies are still unsolved.

We propose a new simulation method for cardiac ultrasound images based on diffusion tensor imaging (DTI) data. The method utilizes the 3D architectures of both cardiac geometry and fiber orientations to simulate the B-mode ultrasound images. This new method not only maintains the accuracy for the myocardial geometries and speckles but also adds the anisotropic intensity distributions in the simulation, which are important for realistically simulating cardiac ultrasound images. In this method, the anisotropy simulation is guided by the 3D cardiac fiber orientations that are acquired from MR-DTI. Its corresponding cardiac geometry is imaged by high-resolution structural MRI and serves as the ground truth of the myocardium. Moreover, the simulated ultrasound images are quantitatively evaluated by comparing the results with real ultrasound images. Additional comparison between the simulated images and the acquired ones of a failed heart was also presented in this study.

This paper is organized as follows: Sec. 2 describes the method of data acquisition, ultrasound simulation, and its evaluations; Sec. 3 describes the results; and discussion and conclusions are in Sec. 4.

2. METHODS

The proposed method contains three steps to simulate cardiac ultrasound images, which are illustrated in Fig. 2. First, the architecture (myocardial geometry and fiber orientations) of real hearts is obtained from high-resolution MRI. Second, the simulated ultrasound images are generated by using the imaged architecture as a guide for the anisotropy simulation. Finally, the simulated images are quantitatively evaluated by comparing the simulation with the acquired ultrasound images.

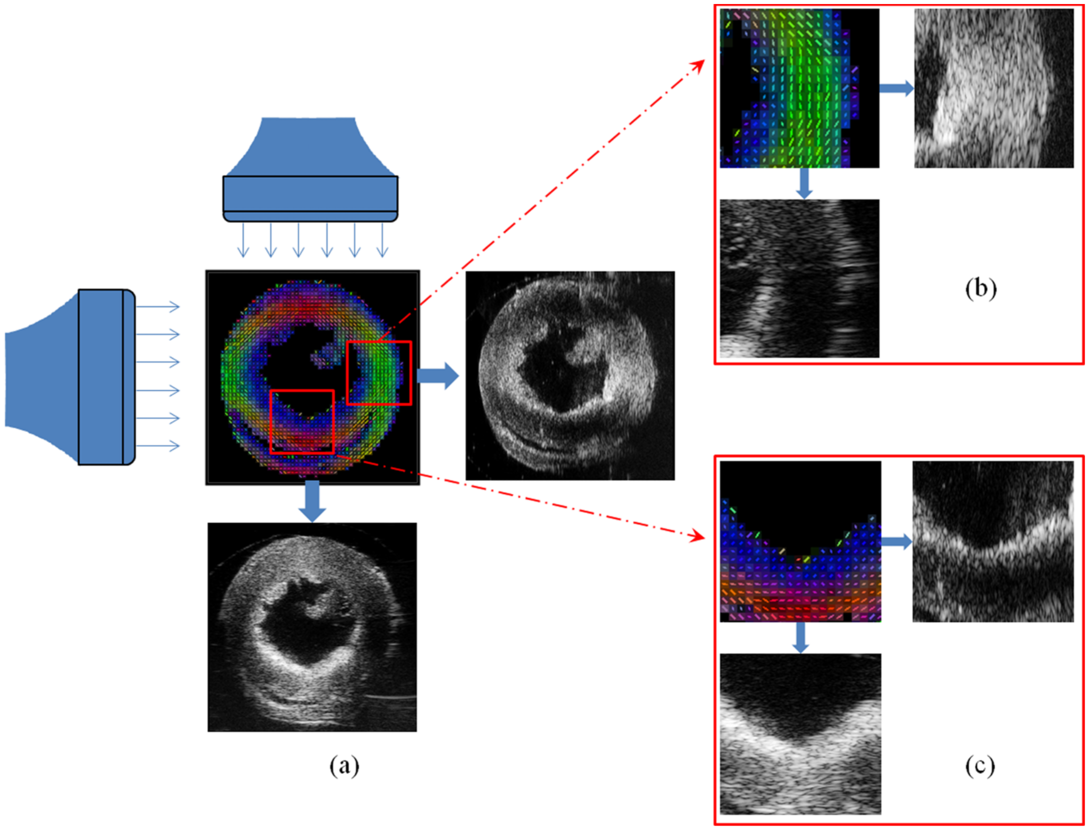

FIG. 1. Relationship between ultrasound intensity and cardiac fiber orientations. (a) Two ultrasound images acquired from both orthogonal directions to image one heart, where middle is the distribution of its fiber orientations. (b) Magnified heart region with main vertical fiber orientations and both corresponding ultrasound images from orthogonal imaging directions. (c) Magnified heart region with main horizontal fiber orientations and both corresponding ultrasound images from orthogonal imaging directions. The enlarged regions in both (b) and (c) demonstrate how different angles between cardiac fiber orientations and ultrasound beam directions affect the ultrasound intensities.

2.A. Cardiac architecture acquisition

2.A.1. DTI data of human heart ex vivo

We used the geometry and fiber orientation data of a human heart in diastole, which were shared by the Cardiovascular Research Grid (CVRG) project.[33,34] It was imaged *ex vivo* by 1.5 T MR scanner (GE Medical System, Wausheka, WI) with a four-element phased array coil. Its spatial resolution was $0.4297 \times 0.4297 \times 1$ mm^3 and its field of view (FOV) was $64 \times 64 \times 100$ mm^3. The DTI scan was performed over 60 h to acquire the cardiac fiber orientations. Note that ultrasound images for this heart were not available.

2.A.2. DTI and ultrasound data of rat heart ex vivo

Therefore, in order to quantitatively evaluate the performance of this proposed method, five ultrasound volumes of fixed rat hearts were imaged by using a Vevo 2100 ultrasound system (FUJIFILM VisualSonics, Inc., Toronto, Canada) with a 30 MHz transducer. B-mode ultrasound images of the hearts in the short-axis view were acquired from apex to base, slice by slice, at a 0.2 mm thickness interval in a FOV of $15.4 \times 20 \times 20$ mm^3. There was no additional time gain compensation (TGC) to the acquisitions. In order to eliminate the susceptibility artifacts, the rat heart samples were completely embedded with agarose. Subsequently, the hearts were imaged by a high-field Biospec 7 T MR scanner (Bruker Corporation, MA) using a RF coil with an inner diameter of 25 mm. Before DTI data acquisitions, anatomical images were acquired by using 3D FLASH sequence with a voxel size of $0.078 \times 0.078 \times 0.156$ mm^3, 3D matrix $= 256 \times 256 \times 128$, TE/TR $= 5/60$ ms, FOV $= 45 \times 45$ mm, NEX $= 4$, and scanning time $= 32$ h. Then, the cardiac fiber orientations were imaged using the spin echo DTI sequence with TR $= 13\,500$ ms, TE $= 27$ ms, b-value $= 0$ and 1000 s/mm^2, gradient directions $= 30$, and 0.234 mm isotropic resolution in a FOV of $30 \times 30 \times 20$ mm^3.

2.A.3. Ultrasound data of rat heart in vivo

Additionally, the ultrasound images of a diseased heart with pulmonary artery hypertension were imaged using an open-chest *in vivo* acquisition approach. With the same ultrasound machine, the *in vivo* images were acquired in the short-axis view and without TGC. After the ultrasound imaging experiment, the fiber orientations were acquired by MR-DTI *ex vivo* on the 7 T MR scanner.

2.A.4. Data preprocessing

After data acquisition, the 3D binary geometric volume of each heart was reconstructed from MRI and ultrasound im-

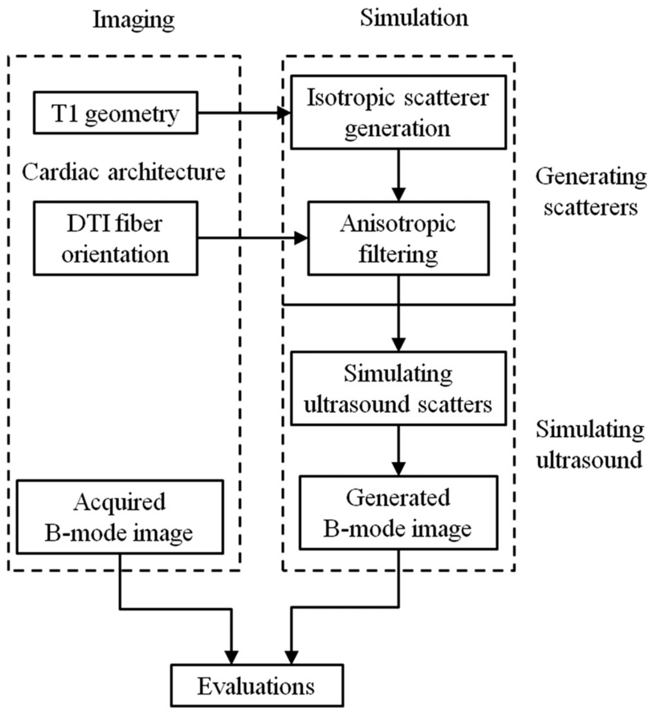

FIG. 2. Flowchart of the whole ultrasound simulation procedure, including cardiac imaging, ultrasound simulation, and quantitative evaluations.

ages, respectively, using a semimanual segmentation method in the Analyze software (AnalyzeDirect, Inc., Overland Park). Next, the tensors of DTI data were decomposed into three eigenvectors, and cardiac fiber orientations were tracked by a determinative method of fractional anisotropy.[26,27,35,36] Since different ultrasound imaging directions lead to different segmental intensities, prior to the simulation, the architectures of rat hearts acquired from MRI were first registered to the corresponding real ultrasound volume. There are two steps for the registration: (1) registration between structural MRI geometries and the real ultrasound ones using a rigid transformation based on the location of the apex and papillary muscles[37] and (2) relocation and reorientation of DTI-derived fiber orientations using the rigid transformation.

2.B. Ultrasound simulation using DTI based anisotropic modeling

2.B.1. Scatterer generation with the anisotropic modeling

First, the whole phantom with the heart inside was modeled as a regular grid of point scatterers with Gaussian distributed backscatter coefficients. The myocardial regions were modeled as grids of point scatterers based on the imaged geometries of the hearts. The scatterer spacing in each phantom was set as an isotropic size, i.e., the same sizes in three dimensions. The backscatter coefficients of these scatterers were initialized as zero-mean Gaussian distributions.

Second, the backscatter coefficient of each scatterer inside the myocardium was enlarged to its 10 times and was then correlated with its corresponding fiber orientation by using a directional smoothing filter with the ellipsoid shape. After this processing, the simulated ultrasound images were generated from the phantom by convolving the PSF with the point scatterers of the phantom using multiplication in the frequency domain (k-space). The backscatter coefficients were correlated by an anisotropic model, which was validated by Crosby *et al.*[23] It was an ellipsoidal Gaussian filter with its principal directions set to match the microstructure orientations of cardiac fibers. The kernel function of this filter is defined as

$$h \propto \exp\left(-\frac{1}{2}\left(\frac{S_1^2}{\sigma_1^2}+\frac{S_2^2}{\sigma_2^2}+\frac{S_3^2}{\sigma_3^2}\right)\right), \tag{1}$$

where S_1, S_2, and S_3 are the variances in the filter space and σ_1, σ_2, and σ_3 are the lengths of the semiprincipal axes of the ellipsoid, as shown in Fig. 3(a). In Ref. 23, this filter was utilized to simulate the ultrasound images of a special designed sample by simplifying filter directions with set

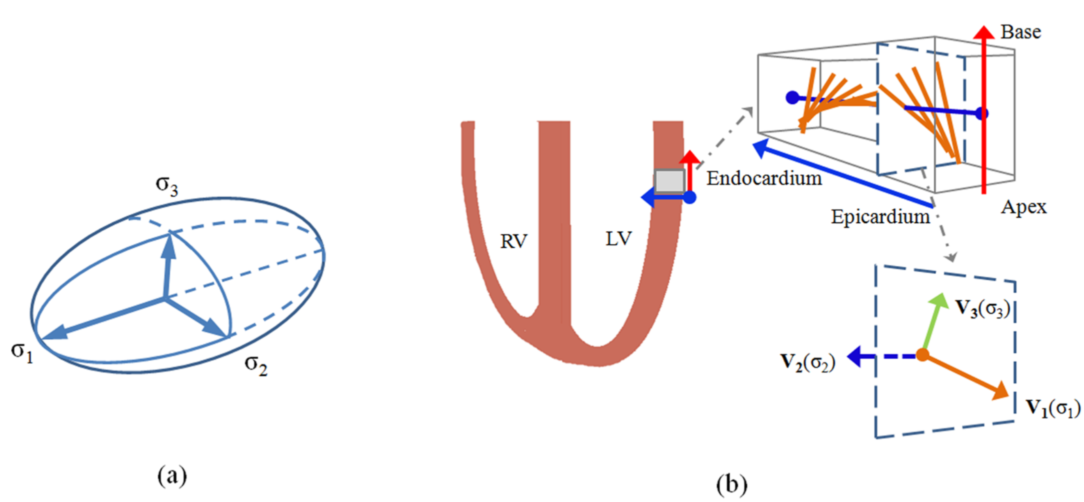

FIG. 3. Relationships among ellipsoid model, DTI eigenvectors, and cardiac fiber orientations. (a) Ellipsoid model, where $\sigma_1 > \sigma_2 > \sigma_3$. (b) Illustrated relationship between three DTI eigenvectors and fiber microstructures: primary eigenvector corresponding to σ_1 indicates the fiber orientation, secondary eigenvector corresponding to σ_2 indicates the sheet direction, and tertiary eigenvector corresponding to σ_3 indicates the sheet norm direction.

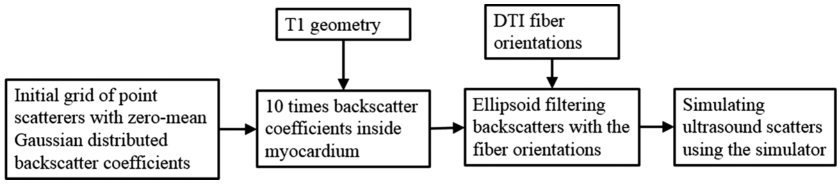

FIG. 4. Flowchart of using structure MRI and DTI data to generate the ultrasound scatterers with the anisotropic modeling.

transmural fiber orientations. However, for the whole heart simulations, the cardiac architecture is more complicated than an excised tissue sample and thus requires an approach to modify the filter directions for each point scatterer.

In the present study, we propose to apply DTI eigenvectors to describe the real microstructure orientations of variable cardiac fibers. The ellipsoid shape at each myocardium grid is then adjusted to match its real fiber orientations represented by these DTI eigenvectors. Using this model, we can generate the anisotropic distributed scatterers within the heart.

We define the three DTI eigenvectors as

$$V_1 = \begin{pmatrix} v_{1x} \\ v_{1y} \\ v_{1z} \end{pmatrix}, \qquad V_2 = \begin{pmatrix} v_{2x} \\ v_{2y} \\ v_{2z} \end{pmatrix}, \qquad V_3 = \begin{pmatrix} v_{3x} \\ v_{3y} \\ v_{3z} \end{pmatrix}. \tag{2}$$

Here, V_1 is the primary eigenvector to indicate the fiber orientation, corresponding to the σ_1 direction. V_2 is the secondary eigenvector to indicate the sheet direction, corresponding to the σ_2 direction. V_3 is the tertiary eigenvector to indicate the sheet norm direction, corresponding to the σ_3 direction. These relationships are shown in Fig. 3(b).

The principal directions of the ellipsoid in Eq. (1) are then reoriented based on DTI eigenvectors following a rotation transformation. For a given rotation matrix $\begin{pmatrix} t_{11} & t_{12} & t_{13} \\ t_{21} & t_{22} & t_{23} \\ t_{31} & t_{32} & t_{33} \end{pmatrix}$, the new point $\begin{pmatrix} x' \\ y' \\ z' \end{pmatrix}$ rotated from point $\begin{pmatrix} x \\ y \\ z \end{pmatrix}$ can be represented as

$$\begin{pmatrix} x' \\ y' \\ z' \end{pmatrix} = T \cdot \begin{pmatrix} x \\ y \\ z \end{pmatrix}. \tag{3}$$

Thus, based on the rotation equation (3), the DTI eigenvectors are considered as the derivation of a rotation T_{DTI} from the unit vectors $X = \begin{pmatrix} 1 \\ 0 \\ 0 \end{pmatrix}$, $Y = \begin{pmatrix} 0 \\ 1 \\ 0 \end{pmatrix}$, $Z = \begin{pmatrix} 0 \\ 0 \\ 1 \end{pmatrix}$ in the filter space. This rotation is calculated as

$$(V_1\ V_2\ V_3) = T_{\mathrm{DTI}} \cdot (X\ Y\ Z), \tag{4}$$

$$T_{\mathrm{DTI}} = (V_1\ V_2\ V_3). \tag{5}$$

Thus, for a point $\begin{pmatrix} x \\ y \\ z \end{pmatrix}$ in the filter space, its corresponding point of the ellipsoidal model (1) is

$$\begin{pmatrix} s_1 \\ s_2 \\ s_3 \end{pmatrix} = T_{\mathrm{DTI}}{}^{-1} \cdot \begin{pmatrix} x \\ y \\ z \end{pmatrix} = (V_1\ V_2\ V_3)^{-1} \cdot \begin{pmatrix} x \\ y \\ z \end{pmatrix}. \tag{6}$$

Then, the weight of point $\begin{pmatrix} x \\ y \\ z \end{pmatrix}$ in the filter space is calculated following Eq. (1). The whole procedure is illustrated in Fig. 4.

2.B.2. Ultrasound simulator

After scatterer generation, a simulator called FUSK was utilized to simulate the ultrasound images because of its fast simulation capability.[12] There are three steps to simulate an image by FUSK. First, each point scatterer of the object is convolved with the PSF of FUSK by multiplication in the frequency domain (k-space). The PSF is constructed in the baseband of the k-space (spatial-frequency domain) and each point scatterer is filtered with a baseband demodulated antialiasing filter. After that, the ultrasound image is generated from the complex demodulated data by the simulated detection, logarithmic compression, and scan-conversion steps. Finally, the image is modified into a grayscale image (0–255). The convolution approach in the k-space makes the simulations much faster than impulse-response based simulators such as Field II but keeps similar accuracies.

2.B.3. Simulation parameter settings

In order to demonstrate the effectiveness of the proposed modeling, ultrasound simulations were first performed on three different datasets: virtual fiber phantoms, the rat hearts, and the human heart. The simulation parameters including grids, modeling, and imaging parameters were set as follows.

2.B.3.a. Ultrasound simulation for fiber phantoms. The virtual phantom contained eight different cardiac fiber objects (range from 0° to 135°) and each object has one set fiber orientation, as shown in Fig. 6(a). The phantom volume size is $14\times20\times5$ mm^3 and its scatterer space is set as 10 μm for both fiber objects and background. The backscatter coefficients of the whole phantom are initialized with a zero-mean Gaussian distribution and then the ones of the fiber objects are set as 10 times of their original values. After that, the backscatter coefficients of the fiber objects are filtered by the anisotropic model based on the corresponding fiber orientations. The corresponding ultrasound image is then generated by a linear array transducer with a central frequency of 30 MHz and the bandwidth of 10 MHz. The corresponding aperture size is 9×5 mm.

2.B.3.b. Ultrasound simulation for rat hearts. During rat heart simulations, the parameters were set to mimic the Vevo MS400 linear array probe used in our experiments. The size of the probe is 20 mm in length and 5 mm in thickness with 256 elements. Its central frequency is 30 MHz and the bandwidth is 10 MHz. The corresponding aperture size is 9×5 mm. Based on the central frequency, the scatterer spaces in the myocardium were all set as 10 μm and were filtered by the anisotropic model based on the DTI-derived fiber orientations. This high scatterer density guarantees that the speckle pattern fully develops. Finally, the ultrasound images are generated after being log-compressed and converted into a gray scale with a gain of 40 and a dynamic range of 45. During this process, no TGC was applied in the simulation because there is no TGC setting applied during our real ultrasound acquisition. All simulated images were set in the short axis due to the acquired images in this imaging view. Moreover, for the purpose of myocardial evaluation, the scatterers inside the backgrounds (without myocardium) of the image are set as zero.

2.B.3.c. Ultrasound simulation for human hearts. For the human heart simulation, a linear array probe with a central frequency of 2.5 MHz and a bandwidth of 0.6 MHz was used. Its aperture size is set as 13×13 mm. Due to its lower central frequency, the scatterer space in the human heart is set as 150 μm, which is much larger than the rat heart. The scatterers inside the myocardium were then modified according to their corresponding DTI-derived fiber orientations and the ones inside the background were kept in their random distributions; this did not distinguish the blood pool and the regions outside the heart. Finally, the ultrasound images are generated after being log-compressed and converted into the gray level with a gain of 45 and a dynamic range of 60. During this process, no TGC was applied in the simulation.

2.C. Proposed evaluation methods

To evaluate the anisotropic distributed intensities in the simulated images, we developed quantitative evaluation methods. We utilize a segmental evaluation method to compare the simulated results with the real ones in each myocardium segment.[29,50–53] The method contains two main steps.

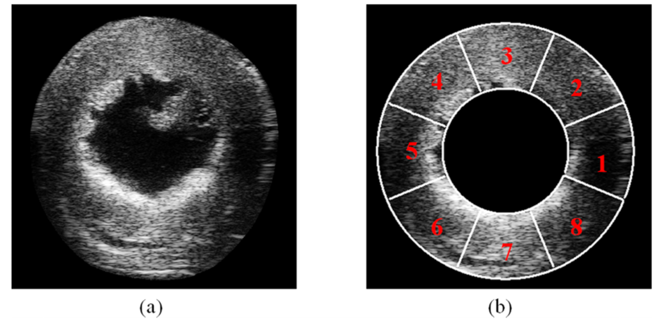

FIG. 5. Illustration of the selected eight segments for the evaluation of ultrasound simulations. (a) Ultrasound image of a rat heart. (b) Divided eight segments of (a), where the white lines indicate the boundaries of the segments.

First, the short axis myocardial region in the image is equally divided into eight segments, which are arranged in a ring, as shown in Fig. 5. This division is based on the variable angles between the ultrasound beam directions and cardiac fiber orientations inside this image.

Second, different statistical parameters are used to analyze the ultrasound intensities of each segment. Mean and standard deviations indicate the average intensity and its variations in each segment. The box plot contains five parameters: the first, second, third quartiles, minimum, and maximum, which are also applied to describe the intensity distributions inside each segment. Moreover, since ultrasound intensities follow Rayleigh distributions,[13] the histogram of each segment is fitted by a Rayleigh distribution. Its probability density function is defined as follows:

$$f(x)=\frac{x}{\sigma^2}e^{-x^2/(2\sigma^2)}, \quad x\geq 0. \tag{7}$$

Here, σ is the scale parameter of a Rayleigh distribution, which is utilized to indicate the intensity distributions of each segment.

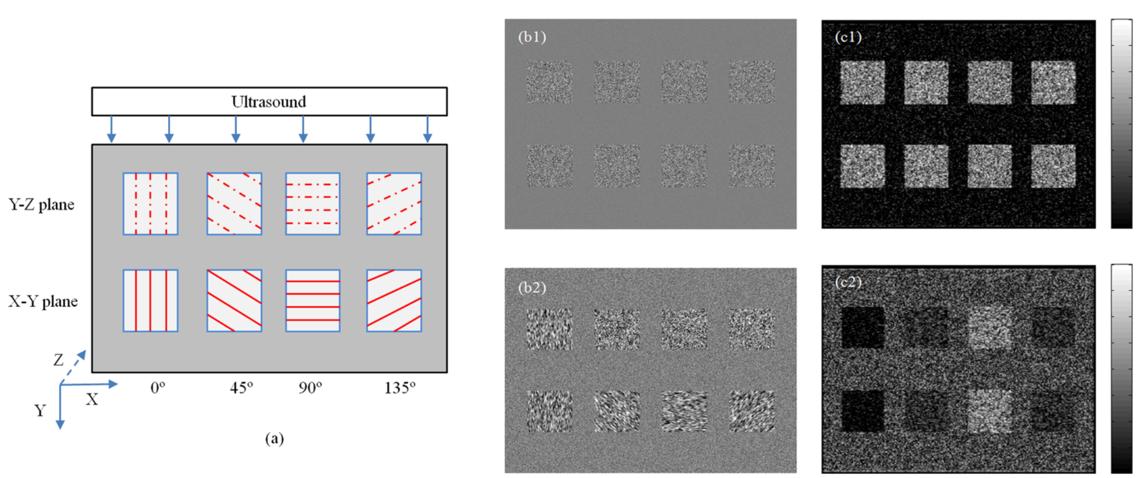

FIG. 6. Ultrasound simulations of a virtual fiber phantom with different fiber orientations. (a) Illustration of the fiber phantom, where the top row indicates the various fiber orientations in the Y–Z plane and the bottom row indicates the ones in the X–Y plane. (b1) Point scatterers randomly distributed. (b2) Point scatterers filtered based on the fiber orientations. (c1) Ultrasound simulation of (b1), showing similar intensities for the eight objects. (c2) Ultrasound simulation of (b2), showing different intensities for the objects with different fiber orientations.

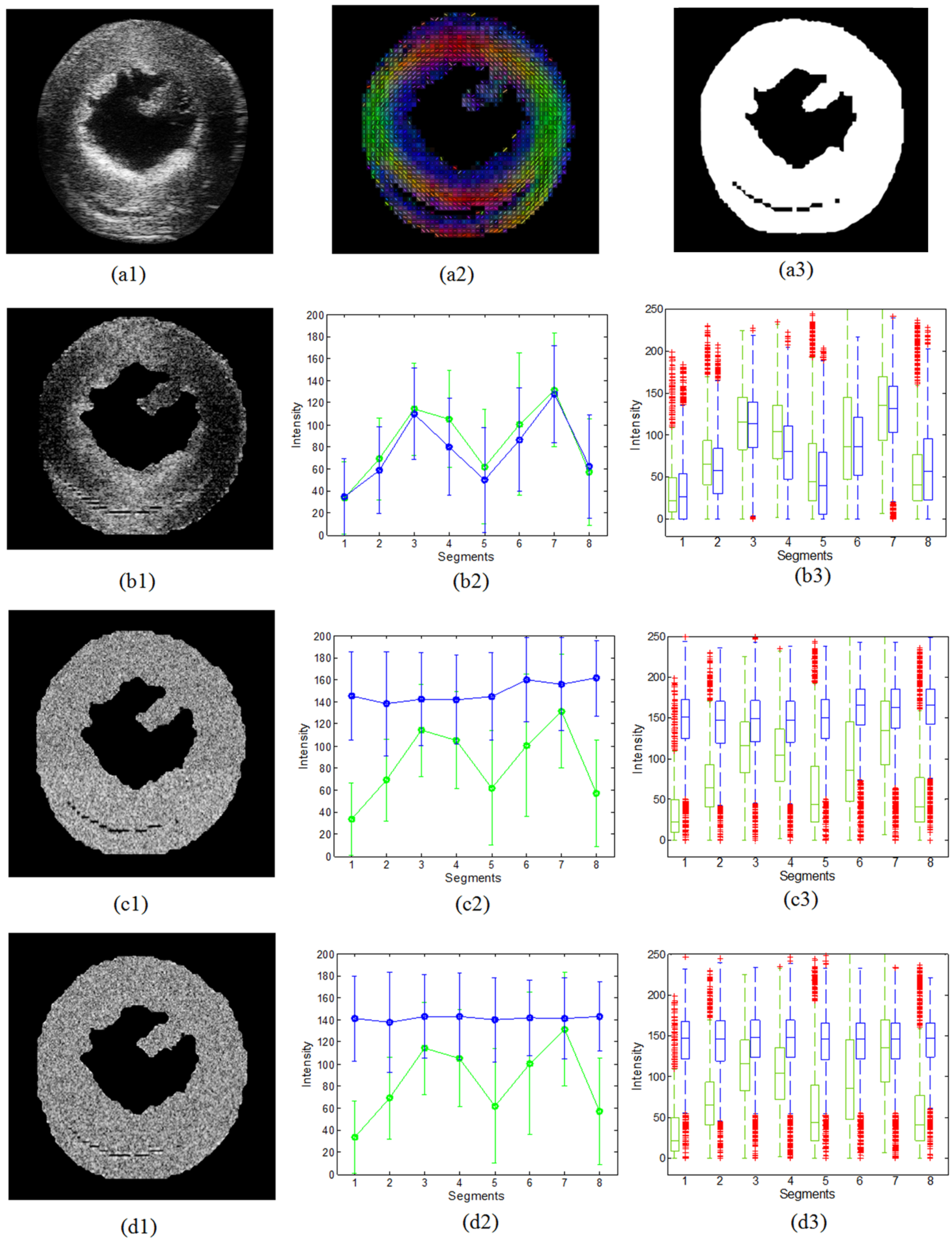

FIG. 7. Comparisons between real cardiac ultrasound images and the simulation results of three different methods. (a1) Real ultrasound image. (a2) Corresponding cardiac fiber orientations from DTI. (a3) Corresponding myocardial geometry from the structure MR. (b1) Simulated ultrasound image with the scatterers filtered by the DTI-derived orientations (M1). [(b2) and (b3)] Mean, median, and quartile intensity comparisons of the eight segments between (a1) and (b1), respectively. (c1) Simulated ultrasound image with the scatterers randomly distributed (M2). [(c2) and (c3)] Mean, median, and quartile intensity comparisons of the eight segments between (a1) and (c1), respectively. (d1) Simulated ultrasound image with the scatterers filtered by the random orientations (M3). [(d2) and (d3)] Mean, median, and quartile intensity comparisons of the eight segments between (a1) and (d1), respectively. Green lines indicate the results of the real image and blue lines indicate the results of the simulated images.

Furthermore, the performance of each parameter of the whole image is evaluated by the average relative error (ARE).[38] The relative error (RE) for each segment is calculated as

$$\mathrm{RE}(x) = \frac{|x - x_0|}{x_0} \times 100, \tag{8}$$

where x is the measured value of the parameter and x_0 is its corresponding real value. Then, the ARE of the image is calculated by averaging the REs of the eight segments. The higher ARE values indicate a higher related error level of the whole image, which means that the simulated result is

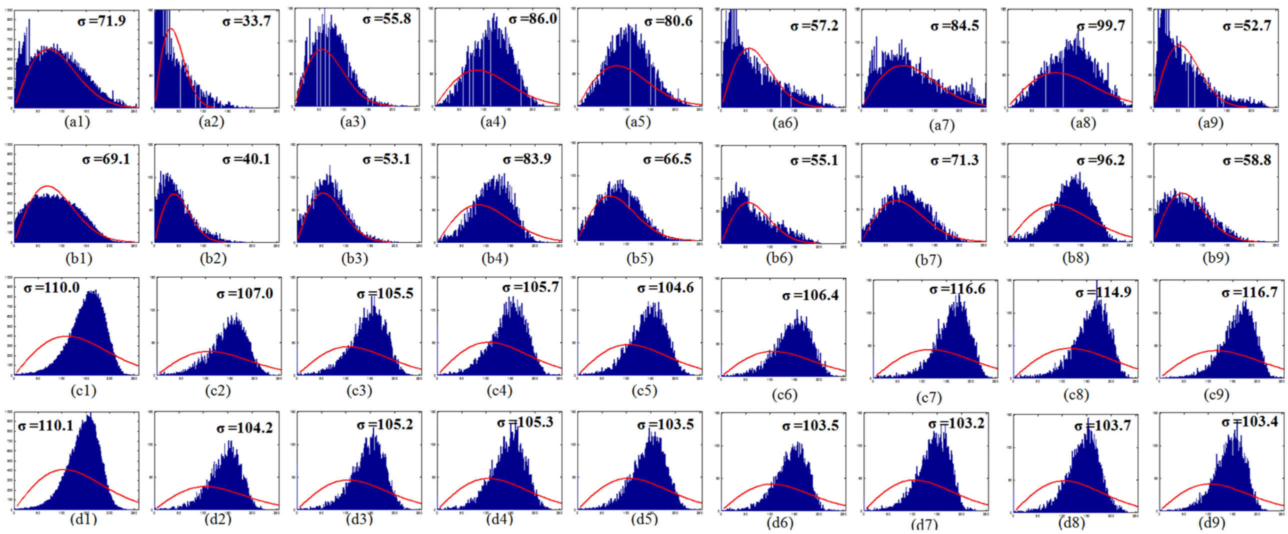

FIG. 8. Comparisons of the histogram distributions of the eight segments in the real and three different simulated ultrasound images. The first row is the results of the real image, the second row is the results of the proposed method M1, the third row is the results of M2, and the fourth row is the results of M3. Column 1 indicates the whole histograms of the four different images, respectively. Columns 2–9 are their corresponding histograms inside the eight evaluation segments, respectively. The red lines inside all subimages indicate the corresponding Rayleigh distributions of the histograms and their scale parameters σ are also listed.

more different from the real image, compared to the simulated images with lower ARE values.

3. RESULTS

3.A. Simulations of virtual fiber phantoms

The simulated ultrasound images of the virtual fiber phantom are shown in Fig. 6. This phantom contains eight objects with different fiber orientations (0°–135°), illustrated in Fig. 6(a). Following the general simulation procedures without the anisotropic modeling, the simulation results in Fig. 6(c1) indicate that the intensities inside the eight objects are similar to each other. In contrast, Fig. 6(c2) demonstrates that the intensities are changed along different fiber orientations of the objects when the anisotropic modeling filters the point scatterers of the phantom. In this simulation, the fiber orientations parallel to the ultrasound beams (0°) lead to the lowest intensities while the perpendicular ones (90°) lead to the highest intensities.

3.B. Simulations and evaluations of rat hearts

The ultrasound images of rat hearts were simulated based on the imaged architectures from anatomical MRI and DTI and then evaluated by comparing with the real ultrasound images from the Vevo scanner. In order to demonstrate the improvement of our proposed method (M1), its performance was compared with other two methods: (i) randomly distributed point scatterers (M2) and (ii) random orientation filtered point scatterers (M3). M2 is a general method utilized in the current cardiac ultrasound simulations. M3 is set as a comparison to demonstrate the necessity of the real connectivity of fiber orientations. These simulations were performed on the same cardiac architecture shown in Figs. 7(a2), 7(a3), and 7(b) with the same grid size and simulation parameters. The simulated results from the three methods (M1–M3) are shown in Figs. 7(b1), 7(c1), and 7(d1). Moreover, these simulated images were divided into eight segments and were quantitatively evaluated by comparing the simulated images with the real ultrasound images shown in Fig. 7(a1). Figures 7(b2) and 7(b3) compares the mean, median, and quartile intensities of the eight segments between the M1 result and the real ultrasound image. The evaluation results of the M2 and M3 methods are shown in Figs. 7(c2) and 7(c3) and Figs. 7(d2) and 7(d3), respectively. These results indicate that the mean and quartiles of the image intensities of the image simulated by M1 are closer to the real ultrasound image as compared to the other two methods. In particular, the M1 result is able to actually simulate the intensity changes in different segments. However, the M2 and M3 methods failed in some segments. Moreover, the box plots of Figs. 7(b3)–7(d3) indicate that most of the

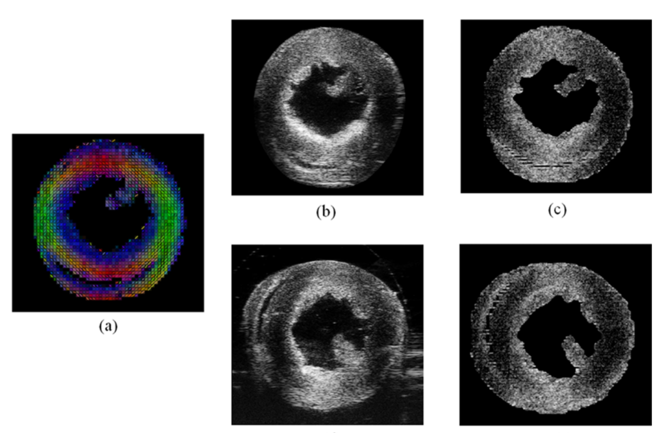

FIG. 9. Simulated ultrasound images from both orthogonal imaging directions of the same rat heart. (a) Cardiac fiber orientations from DTI. (b) Real ultrasound image with vertical beam direction. (c) Simulated result of (b). (d) Real ultrasound image with horizontal beam direction. (e) Simulated result of (d).

TABLE I. The average ARE results of five different parameters from five ultrasound volumes processed by the proposed method and by the other two methods. Ten images for each volume are selected.

Ultrasound data		$\bar{I}$ (%)	σ (%)	Q_1 (%)	Q_2 (%)	Q_3 (%)
Proposed method (M1)	Volume 1	19.0 ± 4.2	18.1 ± 3.3	39.1 ± 7.4	29.8 ± 9.0	25.0 ± 4.1
	Volume 2	21.1 ± 1.6	19.5 ± 0.9	41.8 ± 2.7	28.8 ± 2.7	19.8 ± 0.8
	Volume 3	21.3 ± 2.8	18.7 ± 2.1	33.4 ± 7.6	24.7 ± 3.7	18.8 ± 2.1
	Volume 4	18.3 ± 3.2	17.4 ± 4.2	31.7 ± 7.6	23.1 ± 3.4	21.0 ± 3.6
	Volume 5	15.6 ± 3.0	14.8 ± 1.6	38.2 ± 10.0	22.2 ± 2.8	15.0 ± 1.3
Randomly generated scatterers (M2)	Volume 1	155.4 ± 5.0	113.9 ± 3.5	444.7 ± 34.8	247.7 ± 13.7	126.9 ± 4.9
	Volume 2	113.8 ± 3.8	89.3 ± 3.0	275.6 ± 7.8	144.8 ± 7.6	78.7 ± 3.1
	Volume 3	105.0 ± 13.0	84.3 ± 10.2	219.6 ± 31.9	129.4 ± 17.9	75.2 ± 10.2
	Volume 4	125.4 ± 5.7	92.5 ± 4.9	325.3 ± 12.9	176.1 ± 5.9	93.8 ± 6.3
	Volume 5	161.8 ± 5.1	118.4 ± 4.0	421.8 ± 18.5	223.4 ± 8.7	119.3 ± 4.9
Randomly filtered scatterers (M3)	Volume 1	90.8 ± 9.5	66.4 ± 7.1	237.5 ± 16.8	146.0 ± 9.1	81.3 ± 7.5
	Volume 2	68.9 ± 5.2	55.5 ± 3.7	174.0 ± 9.3	95.3 ± 6.0	50.6 ± 2.8
	Volume 3	70.6 ± 8.1	54.6 ± 5.7	168.9 ± 21.2	98.9 ± 13.4	54.4 ± 5.9
	Volume 4	105.4 ± 9.4	77.1 ± 6.3	273.3 ± 23.6	153.3 ± 14.0	80.5 ± 8.3
	Volume 5	107.0 ± 3.9	79.4 ± 3.1	276.4 ± 13.1	154.2 ± 8.5	83.2 ± 3.9

Note: $\bar{I}$ is the mean intensity of the image; σ is the scale parameter of Rayleigh distribution; Q_1 is the first quartile of the image intensities; Q_2 is the second quartile; Q_3 is the third quartile.

outliers and extreme values of the simulated image by M1 are located in the upper regions, which is similar to the real image. This corresponds to the myocardial speckle pattern, i.e., there are some higher intensity speckles in a lower intensity region. But M2 and M3 fail in this condition and theirs are mostly located in the lower regions. Additionally, the histograms and their fitted Rayleigh distributions were also compared and were presented in Fig. 8. The scale values σ of the fitted Rayleigh distributions indicate that the histograms of the eight segments from the M1 simulation are similar while the other two simulations do not show the segmental changes. Moreover, although the intensity distribution of the whole real ultrasound image has a good correlation to the Rayleigh distribution, some of the divided segments have poorer Rayleigh distributions such as those shown in Figs. 8(a4) and 8(a8). But even so, the simulated ultrasound image can still achieve the similar changes as the real one does in Fig. 8.

Thus, based on these comparisons in Figs. 7 and 8, the segmental similarities between the M1 simulation and the real ultrasound image are higher than those of the other two methods, because M1 captures the intensity changes caused by the cardiac fiber orientations among different segments, as the intensity changes are shown in the real ultrasound image. Figure 9 demonstrates the ability of the proposed method to actually simulate different anisotropic intensities caused by two perpendicular imaging angles of the same heart. Furthermore, the anisotropic intensities of papillary muscles were also appropriately simulated based on their fiber orientations in both simulated images.

Moreover, the ARE evaluations between the simulated ultrasound images by the three methods (M1, M2, and M3) and the real ones from five cardiac volumes are listed in Table I. Ten images from the base of the ventricles to the apex with a 0.4 mm slice space were selected from each volume for the evaluation. Their AREs of five parameters (mean intensity, σ, and first, second, and third quartiles) were averaged as the evaluated errors for each volume. The AREs of our proposed method (M1) are shown as 19% in the mean intensity, 17.7% in the scale parameter of Rayleigh distribution, 36.8% in the first quartile of the image intensities, 25.2% in the second quartile, and 19.9% in the third quartile. In contrast, the evaluated errors of the other two methods M2 and M3 are generally five times more than those of our proposed method.

Additionally, a comparison between the simulated images and the acquired images *in vivo* of a diseased heart is presented in Fig. 10. Based on the *ex vivo* DTI data in Fig. 10(a), the ultrasound image of the myocardium was simulated and is

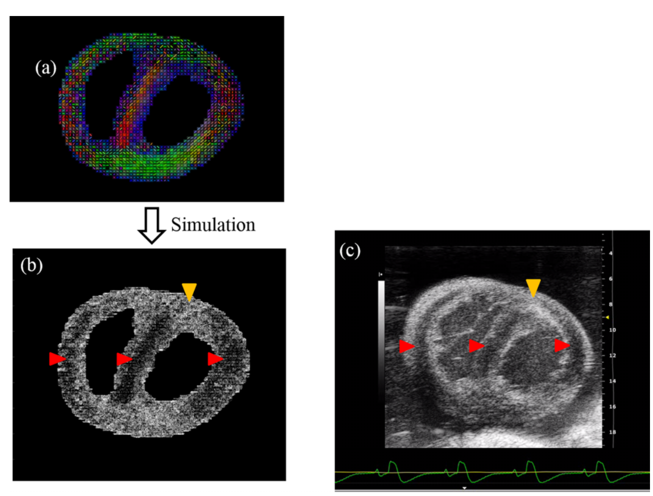

FIG. 10. Comparison between the simulated myocardial ultrasound image and the *in vivo* acquired one of a diseased rat heart with pulmonary artery hypertension. (a) Fiber orientations of the heart from DTI *ex vivo*. (b) Simulated ultrasound image based on DTI data. (c) Acquired ultrasound image *in vivo*. The red arrows indicate the lower intensity regions of myocardium and the yellow ones indicate the higher intensity regions, which are affected by different fiber orientations.

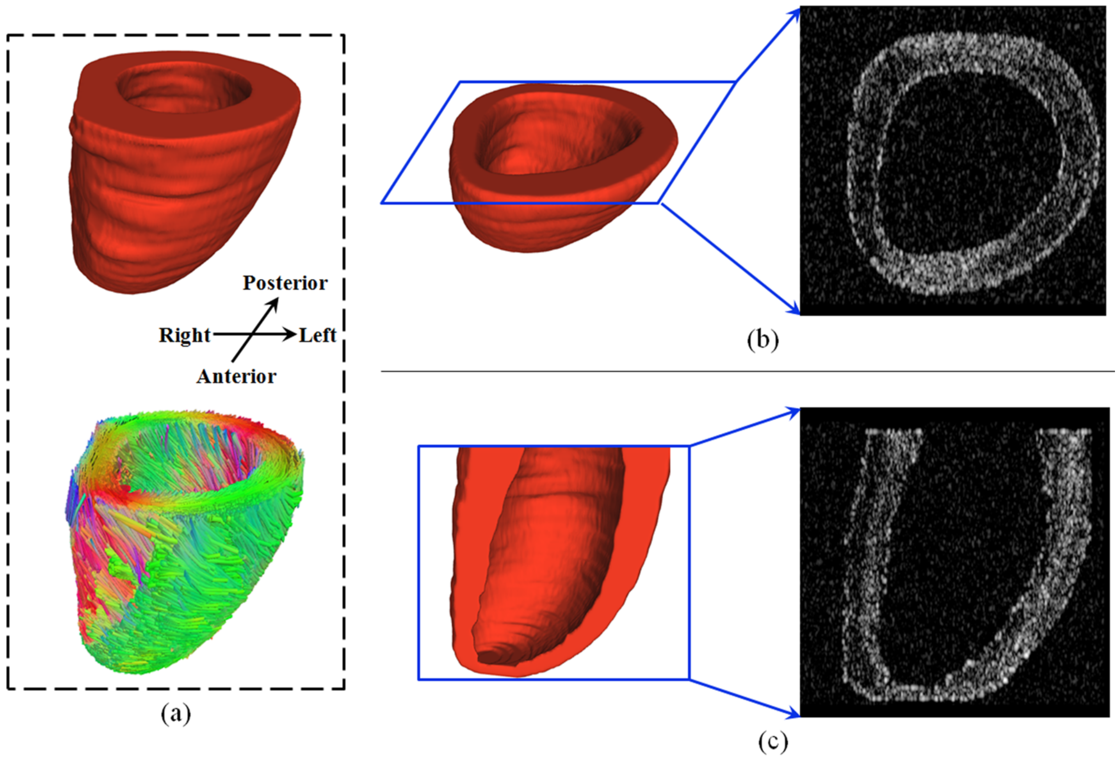

FIG. 11. Simulated myocardial ultrasound images of the left ventricle of a human heart. (a) Architecture of the human heart: the upper row is the geometry from structure MR and the lower row is the fiber orientations from DTI. (b) Simulated ultrasound image from the short axis view. (c) Simulated ultrasound image from the long axis view.

shown in Fig. 10(b). Comparing with the *in vivo* ultrasound image of the same heart, it can be seen that the ultrasound intensities of both images are all lower in the ventricular free walls and septum (pointed by red arrows), where the fiber orientations are parallel to the ultrasound beam directions. On the contrary, the intensities are higher in the upper section of the free wall (pointed by yellow arrows), where the fiber orientations are perpendicular to the ultrasound beam directions.

3.C. Simulations of a human heart

Ultrasound images of a human heart were simulated by the proposed method. Figure 11 presented the simulated myocardium of the left ventricle based on the imaged cardiac architecture, which includes both myocardial geometry and fiber orientations, as shown in Fig. 11(a). The simulated ultrasound image from the short axis view is shown in Fig. 11(b). The simulated ultrasound image from the long axis view is shown in Fig. 11(c). In both simulated images, the intensities indicate the similar anisotropic distributions as the exhibitions of real human ultrasound images due to the cardiac fiber orientations.

3.D. Simulation implementation and computation

The generation of point scatterers and their filtering was implemented by MATLAB (The MathWorks, Inc., Natick, MA). For rat hearts, it took approximately 4 h to generate these point scatterers by parallel computing on 12 cores of a Dell Precision 7600T Workstation (Dell, Inc., Round Rock, TX) and 5 min to simulate one 2D ultrasound image with FUSK. Meanwhile, with the same parallel procedure, it took approximately 1 h to generate point scatterers and 3 min to generate one 2D image for the human heart.

4. DISCUSSION AND CONCLUSION

In this study, we proposed an ultrasound simulation method to simulate the intensity anisotropies inside myocardial regions. These anisotropies are derived from the variable distributions of cardiac fiber orientations.[39,40] This method utilized the DTI-based fiber orientations to simulate the anisotropic effects by processing the point scatterers with an ellipsoidal filter. Although different angles between fiber orientations and ultrasound beam directions lead to different intensities, the proposed simulation method can model these differences of myocardial intensities as the real imaging does.

We also proposed a segment-based evaluation method to measure the difference between the simulated intensities and the real ultrasound images. Different distributions of cardiac fiber orientations lead to the segmental intensity changes in the ultrasound images of the heart. Currently, the general simulation procedures such as the M2 method perform cardiac ultrasound simulations without considering these anisotropies. Our proposed method can achieve better cardiac ultrasound simulation than the other two methods M2 and M3. In this study, we used M3 as an additional comparison to prove that the simulation of the anisotropic effects in ultrasound not only needs the scatterer filtering but also requires the connectivity of real fibers. Our proposed method performs better than the other two methods because they cannot generate the segment differences of intensities as shown in the real images. In contrast, both M2 and M3 perform stable mean intensities in all segments. Furthermore, the quantitative evaluations of different volumes supported this conclusion. During the rat heart simulation with the high-frequency transducer, our simulation uses the small grid size ($\sim$10 μm) and the high transducer frequency (30 MHz) and leads to realistic speckle patterns that are similar to those in real ultrasound images. However, with the same parameters, the simulated speckle patterns of M2 and M3 were different from the real one, as shown in Fig. 7.

Additionally, Fig. 10 shows the comparison between the simulated images and the *in vivo* acquired ones of the same heart, which has heart failure led by pulmonary artery hypertension. In this diseased heart, the geometry changed its shape and the right ventricle became larger than normal one. The results indicated that the simulation method can successfully achieve the similar intensity anisotropy inside the myocardium as the real *in vivo* images did, for the diseased heart. Furthermore, the feasibility of simulating the ultrasound images of a human heart with a clinical ultrasound probe at lower frequency was also demonstrated in the study.

In the future work, the proposed method would be applied to improve the evaluation quality of cardiac ultrasound quantification methods such as myocardial segmentation[41–45] and motion tracking.[15,46] For cardiac segmentation, the myocardial regions with lower simulated intensities support the use of the proposed method in these poor contrast regions, which normally exist in real ultrasound images. The myocardial boundaries acquired by structure MRI at a high resolution are set as the ground truth. Then, the extracted parameters of cardiac function, such as ejection fraction (EF), mass, and volume, can also be quantitatively evaluated. For myocardial motion tracking, this method can be applied to the electromechanical model based simulations to generate more realistic 3D ultrasound sequences.[5] This would be more suitable for the evaluation of optical flow or block-matching based motion tracking, especially when a lower imaging frame rate is used for the tracking.

Although this proposed method performed the anisotropic effects on simulated images, there were still differences between the simulations and the real ones. One reason is that the real images that were acquired from the commercial ultrasound machine were further optimized by postprocessing filters but our results excluded this postprocessing. Thus, the speckles in the real images are smoother than the simulated ones. Moreover, current simulations including both human and rat hearts focused on the simulation of the myocardium only and they were all based on the imaging data of fixed hearts *ex vivo*. For the *in vivo* ultrasound simulation, the motion artifacts, blood flow and papillary muscles, and surrounding organ tissue can also be added to the simulation model. In particular, the right ventricular free wall should be carefully considered because its signals are poor and can be easily affected by the lung or sternum. In this study, we did not incorporate with TGC option because the utilized machine could not output the TGC profiles and it would also cause the changes in real segmental intensities. Additionally, for 3D cardiac ultrasound sequence simulations, the current method is still time-consuming and takes several hours to simulate one volume. That is because the scatterer density would be required for different ultrasound frequencies in order to develop the speckle patterns. Higher frequency usually requires higher scatterer density in order to reduce simulation time. For example, in our case, it was set 10 μm for 30 MHz and 150 μm for 3 MHz. Thus, the simulations, which include both generating scatterers and simulating ultrasound images, should be accelerated by parallel computing, c/c++ programming, etc.

Additionally, the cardiac fiber orientations were acquired by high-resolution DTI in this study. Besides DTI, there are several ultrasound based methods for the estimation of cardiac fiber orientations, which include shear wave imaging, backscatter inversion, and geometry based mapping.[47–49] One potential problem of using shear wave imaging method for this simulation is that it would be difficult to decide the fiber orientations in the 3D geometry, especially when simulating the septum region. Although the echocardiography intensity based method could provide the fiber orientations in 2D images, the ultrasound speckles and other noises would cause errors when estimating complicated 3D fiber structures.

In summary, this study proposed a new ultrasound simulation method to simulate cardiac ultrasound images with the consideration of myocardium anisotropies. The simulation method can be used to provide a quantitative evaluation method for evaluating the accuracy, robustness, and reliability of cardiac ultrasound image processing and analysis such as segmentation, edge detection, and speckle tracking. The simulation method can be also applied to aid cardiac surgery planning and offline training as well as various other applications in cardiac ultrasound imaging.

ACKNOWLEDGMENTS

The authors would like to thank Dr. Rong Jiang in the Emory + Children's Animal Physiology Core in the Department of Pediatrics at Emory University for his technical help on ultrasound imaging. The authors thank the courtesy of Dr. Jonas Crosby, Dr. Torbjørn Hergum, and Dr. Hans Torp in the Department of Circulation and Medical Imaging of Norwegian University of Science and Technology, Norway, for sharing their codes. This work was partially supported by NIH Grant Nos. R01CA156775 and R21CA176684 and a pilot grant from the Children's Heart Research and Outcomes Center of Children's Healthcare of Atlanta.

[a]Author to whom correspondence should be addressed. Electronic mail: bfei@emory.edu; Telephone: 404-712-5649; Fax: 404-712-5689; http://www.feilab.org.

[1]J. A. Jensen and N. B. Svendsen, "Calculation of pressure fields from arbitrarily shaped, apodized, and excited ultrasound transducers," IEEE Trans. Ultrason., Ferroelectr., Freq. Control **39**, 262–267 (1992).

[2]U. R. Abeyratne, A. P. Petropulu, and J. M. Reid, "On modeling the tissue response from ultrasonic B-scan images," IEEE Trans. Med. Imaging **15**, 479–490 (1996).

[3]P. Mohana Shankar, "A general statistical model for ultrasonic backscattering from tissues," IEEE Trans. Ultrason., Ferroelectr., Freq. Control **47**, 727–736 (2000).

[4]A. Elen, H. F. Choi, D. Loeckx, H. Gao, P. Claus, P. Suetens, F. Maes, and J. D'Hooge, "Three-dimensional cardiac strain estimation using spatio-temporal elastic registration of ultrasound images: A feasibility study," IEEE Trans. Med. Imaging **27**, 1580–1591 (2008).

[5]M. De Craene, S. Marchesseau, B. Heyde, H. Gao, M. Alessandrini, O. Bernard, G. Piella, A. R. Porras, L. Tautz, A. Hennemuth, A. Prakosa, H. Liebgott, O. Somphone, P. Allain, S. Makram Ebeid, H. Delingette, M. Sermesant, J. D'Hooge, and E. Saloux, "3D strain assessment in ultrasound (straus): A synthetic comparison of five tracking methodologies," IEEE Trans. Med. Imaging **32**, 1632–1646 (2013).

[6]A. D. Gilliam and S. T. Acton, "Echocardiographic simulation for validation of automated segmentation methods," in *IEEE International Conference on Image Processing* (IEEE, San Antonio, TX, 2013), pp. 2781–2784.

[7]Y. Zhu, X. Papademetris, A. J. Sinusas, and J. S. Duncan, "A coupled deformable model for tracking myocardial borders from real-time echocardiography using an incompressibility constraint," Med. Image Anal. **14**, 429–448 (2010).

[8]C. B. Burckhardt, "Speckle in ultrasound B-mode scans," IEEE Trans. Sonics Ultrason. **25**, 1–6 (1978).

[9]R. F. Wagner, S. W. Smith, J. M. Sandrik, and H. Lopez, "Statistics of speckle in ultrasound B-scans," IEEE Trans. Sonics Ultrason. **30**, 156–163 (1983).

[10]Z. Tao, H. D. Tagare, and J. D. Beaty, "Evaluation of four probability distribution models for speckle in clinical cardiac ultrasound images," IEEE Trans. Med. Imaging **25**, 1483–1491 (2006).

[11]Y. J. Yu and S. T. Acton, "Speckle reducing anisotropic diffusion," IEEE Trans. Image Process. **11**, 1260–1270 (2002).

[12]T. Hergum, S. Langeland, E. W. Remme, and H. Torp, "Fast ultrasound imaging simulation in K-space," IEEE Trans. Ultrason., Ferroelectr., Freq. Control **56**, 1159–1167 (2009).

[13]H. Gao, H. F. Choi, P. Claus, S. Boonen, S. Jaecques, G. H. van Lenthe, G. Van der Perre, W. Lauriks, and J. D'hooge, "A fast convolution-based methodology to simulate 2-D/3-D cardiac ultrasound images," IEEE Trans. Ultrason., Ferroelectr., Freq. Control **56**, 404–409 (2009).

[14]X. Qin and B. Fei, "Measuring myofiber orientations from high-frequency ultrasound images using multiscale decompositions," Phys. Med. Biol. **59**, 3907–3924 (2014).

[15]O. Somphone, M. De Craene, R. Ardon, B. Mory, P. Allain, H. Gao, J. D'Hooge, S. Marchesseau, M. Sermesant, H. Delingette, and E. Saloux, "Fast myocardial motion and strain estimation in 3D cardiac ultrasound with sparse demons," in *IEEE International Symposium on Biomedical Imaging (ISBI)* (IEEE, San Francisco, CA, 2013), pp. 1182–1185.

[16]J. Crosby, B. H. Amundsen, T. Hergum, E. W. Remme, S. Langeland, and H. Torp, "3-D speckle tracking for assessment of regional left ventricular function," Ultrasound Med. Biol. **35**, 458–471 (2009).

[17]M. R. Holland, U. M. Wilkenshoff, A. E. Finch-Johnston, S. M. Handley, J. E. Perez, and J. G. Miller, "Effects of myocardial fiber orientation in echocardiography: Quantitative measurements and computer simulation of the regional dependence of backscattered ultrasound in the parasternal short-axis view," J. Am. Soc. Echocardiography **11**, 929–937 (1998).

[18]W. Kroon, T. Delhaas, P. Bovendeerd, and T. Arts, "Computational analysis of the myocardial structure: Adaptation of cardiac myofiber orientations through deformation," Med. Image Anal. **13**, 346–353 (2009).

[19]H. Chen and T. Varghese, "Three-dimensional canine heart model for cardiac elastography," Med. Phys. **37**, 5876–5886 (2010).

[20]Q. Duan, P. Moireau, E. D. Angelini, D. Chapelle, and A. F. Laine, "Simulation of 3D ultrasound with a realistic electro-mechanical model of the heart," Lect. Notes Comput. Sci. **4466**, 463–473 (2007).

[21]A. Prakosa, M. Sermesant, H. Delingette, S. Marchesseau, E. Saloux, P. Allain, N. Villain, and N. Ayache, "Generation of synthetic but visually realistic time series of cardiac images combining a biophysical model and clinical images," IEEE Trans. Med. Imaging **32**, 99–109 (2013).

[22]M. Alessandrini, H. Liebgott, D. Friboulet, and O. Bernard, "Simulation of realistic echocardiographic sequences for ground-truth validation of motion estimation," in *IEEE International Conference on Image Processing (ICIP)* (IEEE, Orlando, FL, 2012), pp. 2329–2332.

[23]J. Crosby, T. Hergum, E. W. Remme, and H. Torp, "The effect of including myocardial anisotropy in simulated ultrasound images of the heart," IEEE Trans. Ultrason., Ferroelectr., Freq. Control **56**, 326–333 (2009).

[24]M. Aygen and R. L. Popp, "Influence of the orientation of myocardial fibers on echocardiographic images," Am. J. Cardiol. **60**, 147–152 (1987).

[25]E. I. Madaras, J. Perez, B. E. Sobel, J. G. Mottley, and J. G. Miller, "Anisotropy of the ultrasonic backscatter of myocardial tissue .2. Measurements in vivo," J. Acoust. Soc. Am. **83**, 762–769 (1988).

[26]J. G. Mottley and J. G. Miller, "Anisotropy of the ultrasonic backscatter of myocardial tissue .1. Theory and measurements invitro," J. Acoust. Soc. Am. **83**, 755–761 (1988).

[27]D. Recchia, C. S. Hall, R. K. Shepard, J. G. Miller, and S. A. Wickline, "Mechanisms of the view-dependence of ultrasonic backscatter from normal myocardium," IEEE Trans. Ultrason., Ferroelectr., Freq. Control **42**, 91–98 (1995).

[28]B. K. Hoffmeister, A. K. Wong, E. D. Verdonk, S. A. Wickline, and J. G. Miller, "Anisotropy of ultrasonic backscatter from human tendon compared to that from normal human myocardium," in *IEEE Proceedings of Ultrasonics Symposium* (IEEE, Orlando, FL, 1991), pp. 1127–1131.

[29]M. R. Holland, A. Kovacs, S. H. Posdamer, K. D. Wallace, and J. G. Miller, "Anisotropy of apparent backscatter in the short-axis view of mouse hearts," Ultrasound Med. Biol. **31**, 1623–1629 (2005).

[30]R. K. Shepard, D. Recchia, J. G. Miller, and S. A. Wickline, "Ultrasonic anisotropy of backscatter from normal myocardium is view-dependent," Circulation **86**(4) (Suppl. S), 18 (1992).

[31]S. A. Wickline, E. D. Verdonk, and J. G. Miller, "Three-dimensional characterization of human ventricular myofiber architecture by ultrasonic backscatter," J. Clin. Invest. **88**, 438–446 (1991).

[32]M. F. Santarelli and L. Landini, "A model of ultrasound backscatter for the assessment of myocardial tissue structure and architecture," IEEE Trans. Biomed. Eng. **43**, 901–911 (1996).

[33]P. A. Helm, H. J. Tseng, L. Younes, E. R. McVeigh, and R. L. Winslow, "Ex vivo 3D diffusion tensor imaging and quantification of cardiac laminar structure," Magn. Reson. Med. **54**, 850–859 (2005).

[34]D. Rohmer, A. Sitek, and G. T. Gullberg, "Reconstruction and visualization of fiber and laminar structure in the normal human heart from ex vivo diffusion tensor magnetic resonance imaging (DTMRI) data," Invest. Radiol. **42**, 777–789 (2007).

[35]P. Mukherjee, S. Chung, J. Berman, C. Hess, and R. Henry, "Diffusion tensor MR imaging and fiber tractography: Technical considerations," Am. J. Neuroradiology **29**, 843–852 (2008).

[36]F. C. Yeh, V. Wedeen, and W. Y. I. Tseng, "Estimation of fiber orientation and spin density distribution by diffusion deconvolution," NeuroImage **55**, 1054–1062 (2011).

[37]X. Qin, S. Wang, M. Shen, X. Zhang, M. B. Wagner, and B. Fei, "Mapping cardiac fiber orientations from high resolution DTI to high frequency 3D ultrasound," Proc. SPIE **9036**, 90361–90369 (2014).

[38]X. Qin, L. Wu, H. Jiang, S. Tang, S. Wang, and M. Wan, "Measuring body-cover vibration of vocal folds based on high frame rate ultrasonic imaging and high-speed video," IEEE Trans. Biomed. Eng. **58**, 2384–2390 (2011).

[39]D. D. Streeter and D. L. Bassett, "An engineering analysis of myocardial fiber orientation in pigs left ventricle in systole," Anat. Rec. **155**, 503–511 (1966).

[40]D. D. Streeter, H. M. Spotnitz, D. P. Patel, J. Ross, and E. H. Sonnenbl, "Fiber orientation in canine left ventricle during diastole and systole," Circ. Res. **24**, 339–347 (1969).

[41]E. D. Angelini, A. F. Laine, S. Takuma, J. W. Holmes, and S. Homma, "LV volume quantification via spatiotemporal analysis of real-time 3-D echocardiography," IEEE Trans. Med. Imaging **20**, 457–469 (2001).

[42]J. G. Bosch, S. C. Mitchell, B. P. F. Lelieveldt, F. Nijland, O. Kamp, M. Sonka, and J. H. C. Reiber, "Automatic segmentation of echocardiographic sequences by active appearance motion models," IEEE Trans. Med. Imaging **21**, 1374–1383 (2002).

[43]T. Dietenbeck, M. Alessandrini, D. Barbosa, J. D'hooge, D. Friboulet, and O. Bernard, "Detection of the whole myocardium in 2D-echocardiography for multiple orientations using a geometrically constrained level-set," Med. Image Anal. **16**, 386–401 (2012).

[44]P. C. Pearlman, H. D. Tagare, B. A. Lin, A. J. Sinusas, and J. S. Duncan, "Segmentation of 3D radio frequency echocardiography using a spatio-temporal predictor," Med. Image Anal. **16**, 351–360 (2012).

[45]X. Qin, Z. Cong, and B. Fei, "Automatic segmentation of right ventricular ultrasound images using sparse matrix transform and level set," Phys. Med. Biol. **58**, 7609–7624 (2013).

[46]X. Huang, D. P. Dione, C. B. Compas, X. Papademetris, B. A. Lin, A. Bregasi, A. J. Sinusas, L. H. Staib, and J. S. Duncan, "Contour tracking in echocardiographic sequences via sparse representation and dictionary learning," Med. Image Anal. **18**, 253–271 (2014).
[47]W. N. Lee, M. Pernot, M. Couade, E. Messas, P. Bruneval, A. Bel, A. A. Hagege, M. Fink, and M. Tanter, "Mapping myocardial fiber orientation using echocardiography-based shear wave imaging," IEEE Trans. Med. Imaging **31**, 554–562 (2012).
[48]M. L. Milne, G. K. Singh, J. G. Miller, and M. R. Holland, "Echocardiographic-based assessment of myocardial fiber structure in individual, excised hearts," Ultrason. Imaging **34**, 129–141 (2012).
[49]X. Qin and B. Fei, "DTI template-based estimation of cardiac fiber orientations from 3D ultrasound," Med. Phys. **42**, 2915–2924 (2015).
[50]H. Akbari and B. Fei, "3D ultrasound image segmentation using wavelet support vector machines," Med. Phys. **39**, 2972–2984 (2012).
[51]B. W. Fei, Z. H. Lee, D. T. Boll, J. L. Duerk, J. S. Lewin, and D. L. Wilson, "Image registration and fusion for interventional MRI guided thermal ablation of the prostate cancer," in *Medical Image Computing and Computer-Assisted Intervention–MICCAI*, edited by R. E. Ellis and T. M. Peters (Springer, Montréal, Canada, 2003), Vol. 2879, pp. 364–372.
[52]H. Wang and B. Fei, "An MR image-guided, voxel-based partial volume correction method for PET images," Med. Phys. **39**, 179–194 (2012).
[53]B. Fei, X. Yang, J. A. Nye, J. N. Aarsvold, N. Raghunath, M. Cervo, R. Stark, C. C. Meltzer, and J. R. Votaw, "MR/PET quantification tools: Registration, segmentation, classification, and MR-based attenuation correction," Med. Phys. **39**, 6443–6454 (2012).